



Dynamic modeling of the 2004 M_w 6.0 Parkfield, California, earthquake

Shuo Ma,^{1,2} Susana Custódio,¹ Ralph J. Archuleta,¹ and Pengcheng Liu^{1,3}

Received 8 June 2007; revised 27 September 2007; accepted 22 October 2007; published 8 February 2008.

[1] We present two spontaneous rupture models of the 2004 M_w 6.0 Parkfield earthquake constrained by near-source ground motions. We start with a stress drop distribution calculated from a kinematic slip distribution. Using a linear slip-weakening friction law, we utilize trial and error to obtain both the stress conditions and frictional parameters on the fault that produce synthetics consistent with records. The material contrast across the San Andreas Fault is incorporated using different one-dimensional velocity structures on each side of the fault. An approximately constant S parameter of 0.3 and a uniform slip-weakening distance of 0.15 m are used in the dynamic models. In our preferred dynamic model, consistent with the ground motion and GPS, the slip is bounded by seismicity streaks at 5 and 10 km depths, confirming a locked zone at depth. The stress drop is approximately 10 MPa in the hypocentral region and about 2 MPa elsewhere. The material contrast across the fault causes significant normal stress variations (~ 1 MPa), leading to a larger strength drop to the southeast than to the northwest. The main rupture front propagates at nearly a constant subshear rupture velocity ~ 3 km/s in both directions. The total radiated energy determined from the preferred dynamic model is 1.1×10^{13} J, seismic moment is 1.0×10^{18} Nm, and fracture energy is 3.0×10^{13} J. The limited number of aftershocks in the slipped area suggests the important role of stress on the distribution of seismicity in the locked zone.

Citation: Ma, S., S. Custódio, R. J. Archuleta, and P. Liu (2008), Dynamic modeling of the 2004 M_w 6.0 Parkfield, California, earthquake, *J. Geophys. Res.*, 113, B02301, doi:10.1029/2007JB005216.

1. Introduction

[2] In this paper, we present a dynamic source model of the 2004 M_w 6.0 Parkfield earthquake. The rupture is modeled as a spontaneously propagating crack under the simultaneous control of the stress and frictional resistance on the fault. Contrary to kinematic models that contain mechanical inconsistencies, the propagation of dynamic ruptures evolves naturally from solving the elastodynamic equations while satisfying a well-defined friction law on the fault. Dynamic rupture models constrained by ground motion have been attempted for several earthquakes: 1979 Imperial Valley earthquake [Favreau and Archuleta, 2003], 1992 Landers earthquake [Olsen et al., 1997; Peyrat et al., 2001], 1994 Northridge earthquake [Nielsen and Olsen, 2000; Ma and Archuleta, 2006], 2000 Tottori, Japan, earthquake [Dalguer et al., 2003; Peyrat and Olsen, 2004], and the 2002 Denali earthquake [Dunham and Archuleta, 2004].

[3] Dynamic rupture models of earthquakes, incorporating simple fault friction, have provided new insights into the

physics of earthquakes. Relevant to Parkfield, dynamic rupture simulations on a bimaterial interface with a slip-weakening friction law [Ida, 1972; Palmer and Rice, 1973] have demonstrated that the material contrast across a fault can significantly affect the rupture propagation [e.g., Harris and Day, 1997, 2005]. The asymmetry in the material properties prevents the normal stress from being a constant on the fault. If we define the slip direction of the more compliant material to be positive and of the more rigid material to be negative, for subshear ruptures the normal stress variation is compressive ahead of rupture front but tensile behind it, and vice versa in the negative direction. The normal stress variations on the fault essentially lead to the asymmetry in the rupture propagation speed, amplitude of slip rate function, and potentially the ground motion along each rupture direction. A lab experiment [Xia et al., 2005] has confirmed the bilateral rupture propagation and asymmetry in rupture speeds seen by Harris and Day [1997, 2005]. The material contrast across the fault has also been used to explain the asymmetry in the observed damage pattern of fault zone [Dor et al., 2006a, 2006b] and the asymmetry in aftershock distributions of microearthquakes [Rubin and Ampuero, 2007].

[4] These results have important implications for Parkfield earthquakes, where the velocity structure is characterized by a contrast across the San Andreas Fault (SAF) with generally faster material (Salinian granitic rocks) on the southwest side of the fault and slower material (Franciscan

¹Department of Earth Science and Institute for Crustal Studies, University of California, Santa Barbara, Santa Barbara, California, USA.

²Now at the Department of Geophysics, Stanford University, Stanford, California, USA.

³Now at U.S. Bureau of Reclamation, Denver, Colorado, USA.

assemblage rocks) on the northeast side [Eberhart-Phillips and Michael, 1993; Thurber et al., 2006]. Following the definition of rupture direction in a bimaterial context, in Parkfield the southeast direction would correspond to the positive direction and northwest to the negative direction. It has been argued that the rupture would propagate preferably to the positive direction [Andrews and Ben-Zion, 1997; Ben-Zion and Andrews, 1998; Cochard and Rice, 2000; Ranjith and Rice, 2001] based on models with constant friction on the fault. These models ignored the dominant effect of stress breakdown process [Harris and Day, 2005; Rubin and Ampuero, 2007]. The 2004 Parkfield earthquake propagated predominantly to the northwest [Langbein et al., 2005], which is the negative direction. Though there are still debates on whether or not the material contrast across the fault controls the direction of rupture propagation [Harris and Day, 2005, 2006; Ben-Zion, 2006], the material contrast across the SAF in the Parkfield region potentially plays an important role in the dynamics of the rupture process.

[5] The rupture process of the 2004 Parkfield earthquake has been inverted kinematically from the strong motion data [Custódio et al., 2005; Liu et al., 2006] and combined strong motion data and Global Positioning System (GPS) data [Langbein et al., 2005; Custódio et al., 2007]. A coseismic slip distribution has also been obtained by inverting the GPS and Interferometric Synthetic Aperture Radar (InSAR) data simultaneously [Johanson et al., 2006] and the GPS data alone [Murray and Langbein, 2006]. Fletcher et al. [2006] inferred the velocity of rupture propagation of this earthquake from observations of ground accelerations recorded at a short-baseline seismic array (UPSAR) located about 12 km west of the epicenter. Borchardt et al. [2006] estimated the apparent rupture velocity at the surface from the recorded fault-parallel and fault-normal displacement pulses.

[6] In the following, we will incorporate the material contrast across the SAF in the dynamic modeling of the 2004 Parkfield earthquake. To infer the stress conditions and frictional parameters on the fault, we will first calculate the stress drop from the inverted slip model of Custódio et al. [2005] using a static finite element method. We assume an approximately constant S parameter ($S = \frac{\sigma^y - \sigma^0}{\sigma^0 - \sigma^d}$, where σ^y , σ^0 , and σ^d are the yield stress (stress at which slip initiates), initial stress, and dynamic frictional stress, respectively, introduced by Andrews [1976] and Das and Aki [1977]) to get the strength excess $\sigma^y - \sigma^0$. With the use of a slip-weakening friction law [Ida, 1972; Palmer and Rice, 1973], we modify the stress drop, the S parameter, and the critical slip-weakening distance by trial-and-error until the dynamic rupture model generates synthetics that can explain the recorded ground motions near the fault. We will present two rupture models that explain the ground motion well, both of which will be independently checked against the GPS observations.

[7] In our preferred dynamic model, the rupture area is nearly a rectangle delineated by aftershocks between 5 km and 10 km depth [Thurber et al., 2006]. The rupture propagates bilaterally with nearly constant rupture velocities. The southeastward rupture dies out soon after the initiation of the earthquake and the rupture mainly propagates to the northwest, which is entirely determined by the derived stress conditions and friction on the fault in the given velocity structure. We will then compare the similar-

ities and differences in the rupture parameters (slip, rupture time, and risetime) arising from our preferred dynamic model and the kinematic model of Custódio et al. [2005]. In addition, we will estimate the radiated energy and fracture energy of the Parkfield earthquake from both dynamic models following the method of Favreau and Archuleta [2003] and Ma and Archuleta [2006], and discuss the role of stress in the distribution of seismicity on fault.

2. Dynamic Modeling

[8] Using a finite element method [Ma and Liu, 2006] we solve the equations of motion in a three-dimensional (3-D) linear elastic isotropic medium

$$\begin{aligned} \rho \ddot{u}_i &= \sigma_{ij,j} + f_i, \text{ and} \\ \sigma_{ij} &= \lambda u_{k,k} \delta_{ij} + G(u_{i,j} + u_{j,i}), \end{aligned} \quad (1)$$

where u is the displacement, σ is the stress tensor, f is the body force, ρ is the density of the medium, λ and G are Lamé's constants, δ_{ij} is the Kronecker Delta, and a comma denotes differentiation. Summation over repeated indices is assumed. The fault is modeled as an internal boundary, where the traction is governed by a friction law. The traction change with respect to the initial stress state on the fault essentially gives the driving force of the system.

[9] We discretize equation (1) by using 8-node hexahedral elements in space and a central-difference scheme in time. The finite element method [Ma and Liu, 2006] uses a one-point integration scheme with both viscous and stiffness hourglass control. A split-node scheme [Andrews, 1999; Day et al., 2005] is used to model the fault boundary conditions.

[10] Owing to the simple fault geometry we have chosen (described below), we use a regular mesh with 8-node cubic elements everywhere. Thus the whole implementation of the finite element scheme with one-point integration is very similar to the finite difference scheme of Day [1982b] and Day et al. [2005], except that we do not include artificial viscosity in the medium. The artificial viscosity used in the simulation of Harris and Day [1997, 2005] made the rupture on a bimaterial interface well-posed. However, the ill-posedness mostly occurs in the positive direction [Ranjith and Rice, 2001; Cochard and Rice, 2000], and the problem is well-posed in the negative direction. The 2004 Parkfield earthquake mostly ruptured in the negative direction; the rupture length in the positive direction is too small for the ill-posedness to affect the rupture. The element size is 100 m in order to simulate synthetics up to 1 Hz in the velocity structure we choose. The entire computational domain is 80 km (along strike) \times 50 km (perpendicular to strike) \times 30 km (along depth). The time step is 0.012 s. The simulation is run for 40 s. We use simple dampers [Lysmer and Kuhlemeyer, 1969] along the mesh edges except at the free surface in order to prevent wave reflections from contaminating the interior solution.

[11] Precise aftershock locations of the 2004 Parkfield earthquake delineate a complex fault geometry in the Parkfield region [Thurber et al., 2006; Simpson et al., 2006]. Below a depth of 6 km, aftershocks fall on a straight vertical fault plane, presumably the SAF. However, aftershock

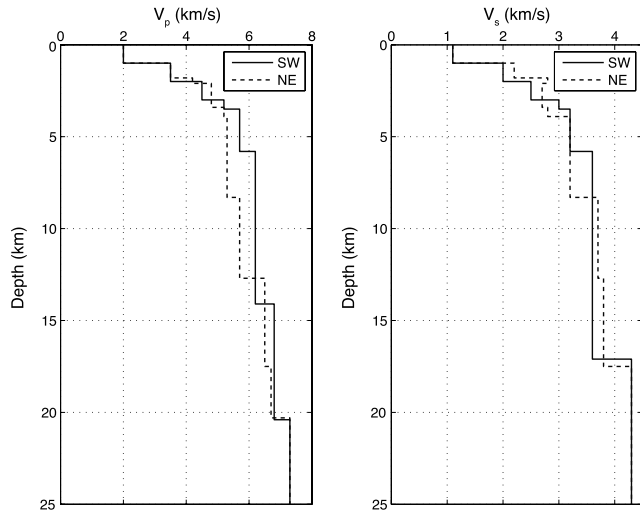


Figure 1. Plot of seismic wave velocities as a function of depth. Material contrast across the San Andreas Fault is represented by different one-dimensional velocity structures on each side of the fault.

locations in the upper 6 km delineate two fault strands, where one strand warps to the northeast and is potentially connected to the surface trace of the SAF and the other is extended vertically to the Southwest Fracture Zone (SWFZ). This fault geometry has been used to invert the coseismic and postseismic slip of the Parkfield earthquake [Murray and Langbein, 2006]. However, most coseismic slip from strong ground motion inversions occurs below 6 km [e.g., Custódio *et al.*, 2005; Liu *et al.*, 2006] and the shallowest asperity toward the northwest in the inversion of Custódio *et al.* [2005] and Liu *et al.* [2006] is located where the two fault strands collapse onto one single SAF fault plane [Simpson *et al.*, 2006]. Therefore we simplify the fault geometry and model the 2004 Parkfield earthquake as a vertical strike-slip earthquake. Any slip shallower than 6 km in our model can be interpreted as taking place on the strand connecting to the SWFZ. The fault is 40 km along strike and 15 km along dip. Because no significant surface slip was observed immediately after the earthquake, the top of the fault is set to a depth of 0.5 km. The strike of the fault is chosen to be 140° following the pattern of aftershocks. The hypocenter is located at (35.817°N , 120.365°W) and 8.1 km depth. These parameters are similar to those used by Custódio *et al.* [2005].

[12] We take into account the material contrast by using a simplified velocity model with different one-dimensional velocity structures on each side of the fault (see Table 1 and Figure 1). This velocity model is interpolated from the 3-D velocity model of Eberhart-Phillips and Michael [1993] and Thurber *et al.* [2003] and is identical to the one used by Custódio *et al.* [2005] in their kinematic inversion. At the hypocentral depth the shear wave velocity is 3.6 km/s and 3.2 km/s on the southwest and northeast side of the fault, respectively, giving rise to a 12.5% velocity contrast across the fault.

[13] Friction laws govern the rupture initiation, propagation and healing. In our dynamic modeling we use a slip-weakening friction law [Ida, 1972; Palmer and Rice, 1973] that was first used by Andrews [1976] to avoid the stress

singularity and to account for finite energy absorption at the crack tip. It is regarded as a reasonable representation of the breakdown process during high-speed seismic ruptures and has been widely used in dynamic rupture modeling [e.g., Day, 1982b; Harris and Day, 1997; Olsen *et al.*, 1997; Peyrat *et al.*, 2001; Day and Ely, 2002; Favreau and Archuleta, 2003; Ma and Archuleta, 2006]. In this simple friction law, the friction coefficient μ is a function of slip alone and drops linearly from the static friction coefficient μ_s to the dynamic frictional coefficient μ_d over a characteristic distance D_c . It remains at the dynamic friction coefficient μ_d when the slip exceeds the slip-weakening distance D_c (Figure 2). The magnitude of yield stress and dynamic frictional stress is given by $\mu_s\sigma_N$ and $\mu_d\sigma_N$, respectively, where σ_N is the normal stress. Note that the normal stress σ_N can be time-dependent. In order to use this friction law, we need to know the distribution of initial stress, static and dynamic frictional coefficients, slip-weakening distance and initial normal stress everywhere on the fault.

[14] To infer the stress conditions on the fault, we start with the slip distribution of Custódio *et al.* [2005]. We first linearly interpolate the kinematic slip onto the much finer grid that we use for the dynamic rupture simulation and assume that slip is along strike. We use a static finite element method to calculate the static stress drop in the velocity structure (Table 1) by prescribing the slip as a displacement boundary condition and ensuring the continuity of tractions across the fault. The calculated static stress drop is somewhat noisy because the static stress drop is related to the spatial derivatives of slip. We slightly smoothed the calculated static stress drop with a spatial average of 1 km (Figure 3). The static stress drop distribution correlates very well with the slip distribution (as expected, because they are uniquely related to each other through the equations of static elasticity). We assume a uniform dynamic friction σ^d of 18 MPa and that the dynamic stress drop is equal to the static stress drop. The shear stress on the fault is assumed along strike. Thus

Table 1. One-Dimensional Velocity Structure

Thickness, km	Density, kg/m ³	V _p , m/s	V _s , m/s
<i>SW</i>			
1.0	2000	2000	1100
1.0	2300	3500	2000
1.0	2300	4500	2500
0.5	2500	5200	3000
2.3	2700	5700	3200
8.3	2700	6200	3600
3.0	2800	6800	3600
3.3	2800	6800	4300
-	2800	7300	4300
<i>NE</i>			
1.0	2000	2000	1100
0.8	2300	3500	2200
0.3	2300	4200	2800
1.3	2300	4800	2700
0.5	2300	5200	2800
4.4	2700	5300	3200
4.4	2800	5700	3700
4.8	2800	6500	3800
2.8	2800	6700	4300
-	2800	7300	4300

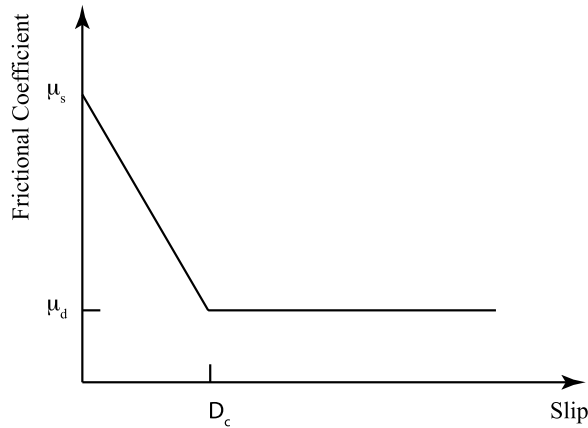


Figure 2. Linear slip-weakening friction law. As the slip initiates, the frictional coefficient decreases linearly with slip over a characteristic slip-weakening distance D_c .

the initial stress σ^0 can be obtained by the sum of the calculated stress drop $\Delta\sigma$ and dynamic friction σ^d , that is, $\sigma^0 = \Delta\sigma + \sigma^d$. Note that only the stress change with respect to the initial stress affects the dynamics of rupture and in turn the ground motions; that is, the absolute stress level is not very important. The absolute stress level on fault could affect the temporal rake rotations [Guatteri and Spudich, 1998]. Our chosen stress level would imply that the slip direction is mainly along strike. This original initial stress distribution is a starting model, which we will adjust by adjusting the calculated stress drop $\Delta\sigma$ through trial and error so that the synthetics can match the data. We assume a constant initial normal stress σ_N^0 of 60 MPa over the whole fault, which gives a uniform dynamic friction coefficient μ_d of 0.3 on the fault. For simplicity, we assume a uniform distribution of the slip-weakening distance D_c on the fault. By trying different values, we find that $D_c = 0.15$ m best fits the near-source ground motions.

[15] To get the distribution of static frictional coefficient on the fault, we use a constant S parameter [$S = \frac{\sigma^s - \sigma^0}{\sigma^0 - \sigma^d} = \frac{\mu_s \sigma_N^0 - (\Delta\sigma + \sigma^d)}{\Delta\sigma}$]. With the assumed parameters ($\sigma^d = 18$ MPa, $\sigma_N^0 = 60$ MPa), we can calculate the static frictional coefficient μ_s from the stress drop $\Delta\sigma$ and the S parameter. By trial and error, we successively modify both the stress drop $\Delta\sigma$ and the S parameter on the fault and dynamically rupture the fault until the synthetics match the near-source ground motions. The rupture is highly sensitive to the stress distribution on the fault. Depending on the different distributions of stress drop and strength excess, the rupture can either stop too early, break a much larger fault area than it should, or propagate along drastically different paths. However, after several trial runs we found two distributions of stress drop and strength excess that are able to explain the ground motion observations (Models A and B in Figure 4).

[16] The stress drop distribution of Model A is very similar to that shown in Figure 3 except that we added 1.0 MPa to all of the fault area with positive stress drop in order to generate the correct amplitudes of ground velocity. In addition, we filled several holes of negative stress drop (Figure 3) such that there are no strong barriers to the rupture propagation in the middle of rupture area. We used a constant S parameter of 0.3 to get the static frictional

coefficient μ_s for regions with positive stress drop. For regions with negative stress drop, we simply use $\mu_s = 0.33$, which is arbitrary. We just choose a value that is slightly higher than the dynamic friction coefficient $\mu_d = 0.3$. It does not affect the rupture propagation much because the negative stress drop is only on the edges of the rupture area. Note that the normal stress varies during the rupture propagation due to the material contrast. In Figure 4 we plot the strength excess at each point during the rupture process. The higher strength excess on the edge of rupture area is due to the negative stress drop, not a high yield stress. For the areas without slip, both the stress drop and strength excess are undetermined.

[17] In Model B the rupture area is approximately a rectangle 30 km \times 5 km. We keep stress drop and strength excess within the rectangle similar to Model A and remove all the features outside the rectangular area. In this model, the area of faulting is basically bounded by the microseismicity, as discussed later. We use a small negative strength excess of -0.5 MPa on a 0.5-km radius circular patch around the hypocenter to nucleate the rupture (see Figure 4). In both Models A and B, stress drop is approximately 10 MPa on a roughly rectangular asperity (5 km along strike \times 2 km along dip) around the hypocenter where the kinematic inversion places the largest amount of slip. In other asperities outside the hypocenter, stress drop is on the order of 2 MPa. Near the edge of the rupture area, the stress drop smoothly transitions to negative.

[18] It has been proposed that fault rheology likely plays a major role in determining the rupture extent of Parkfield earthquakes [e.g., Waldhauser et al., 2004; Bakun et al., 2005; Fletcher et al., 2006; Johanson et al., 2006; Langbein et al., 2006; Murray and Langbein, 2006; Thurber et al., 2006] based on the collocation of aftershocks of both the 1966 and 2004 earthquakes and background seismicity [Waldhauser et al., 2004; Thurber et al., 2006]. Most aftershocks of the 2004 Parkfield earthquake that occur near the hypocenter lie amazingly along two horizontal streaks around 5 km and 10 km depths, respectively [Thurber et al., 2006]. These aftershock streaks can be interpreted as marking the transition between creeping and locked regions of the fault [Nadeau et al., 1995]. Aftershocks in the area between the streaks are, however, significantly less abundant. This is the primary reason for constructing Model B, which only breaks the area outlined by the aftershocks, that is, between 5 km and 10 km depth. We test the hypothesis of whether or not the slip bounded by aftershocks can explain the ground motion and GPS observations.

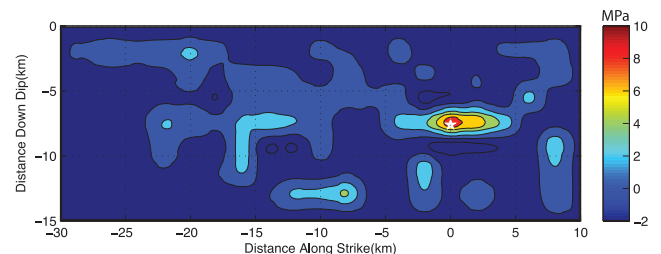


Figure 3. Distribution of the static stress drop calculated from the slip distribution of Custodio et al. [2005]. The star denotes the hypocenter.

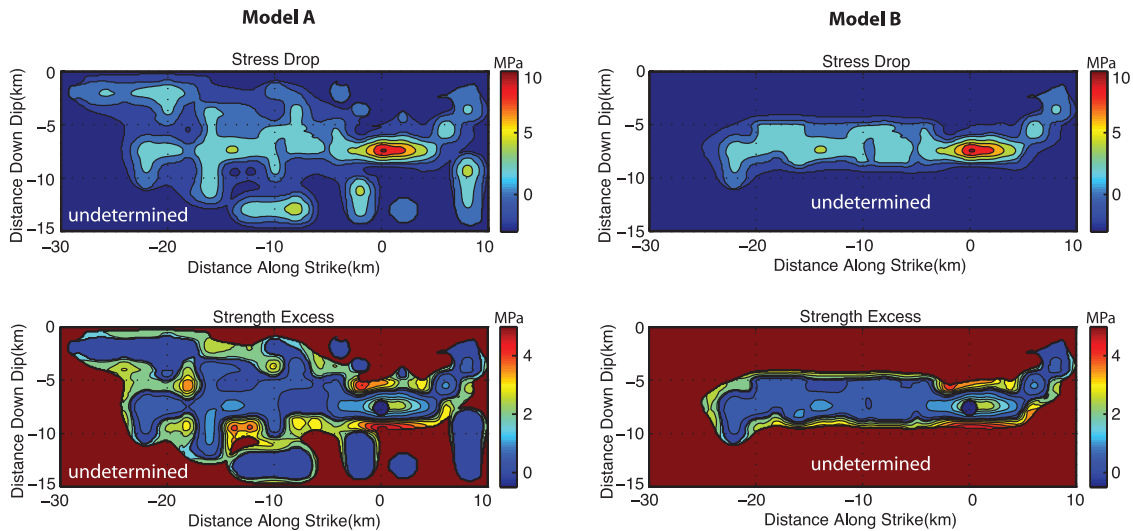


Figure 4. Two distributions of stress drop and strength excess used in the spontaneous rupture modeling of the 2004 Parkfield earthquake are mapped onto the fault plane. Model B is our preferred model. The stress drop smoothly transitions to be negative at the boundary of the slipped area, leading to a high strength excess which stops the rupture. In the region without slip, both the stress drop and strength excess are undetermined. A negative strength excess -0.5 MPa in a 0.5 km-radius patch nucleates the rupture.

[19] We will show later that Model B generates surface displacements much more consistent with GPS observations than Model A. Note that the GPS data have not been used to constrain the stress conditions and fault friction, so they provide an independent check of each dynamic model. Though both models can explain the ground motion well, we prefer Model B because it produces better fits to the GPS data.

[20] We allow the fault to spontaneously rupture with the determined distributions of stress drop and strength excess (Figure 4) in the velocity structure (Table 1). Rake is allowed to rotate. Each point on the fault obeys the slip-weakening friction law. Slip starts when the shear stress exceeds the yield stress. Then shear stress drops down to the dynamic friction as a function of slip until slip reaches the slip-weakening distance D_c (0.15 m). The fault then keeps sliding at the dynamic friction. The criterion for each point to stop sliding closely follows *Andrews* [1999]. At each time step and for each point on the fault, we compute a traction \mathbf{T}^* that will cause the slip rate to be zero at the next time step. If, at a point on the fault, the magnitude of the traction \mathbf{T}^* is smaller than that of the dynamic friction, we will set the traction at this point at current time step to be \mathbf{T}^* and the point will stop sliding at next time step. This point may start sliding again if the shear stress exceeds the dynamic friction. In Figure 5, we plot snapshots of slip rate, shear stress change, normal stress change, and slip at 0.9 s intervals for our preferred model. The slip rate, shear stress, and slip are all along-strike components.

[21] What we observe in Model B is that the rupture initiates at the hypocenter and propagates with a fast rupture velocity both to the northwest and southeast along a narrow strip accommodating the large stress drop. The asymmetry in the amplitude of slip rate in the two rupture directions (larger in the southeast direction) due to the material contrasts is clearly seen in the first few seconds. The

southeast propagating rupture front terminates at about 3.6 s. The northwest rupture propagates horizontally along strike at an almost constant speed. The rupture is crack-like but confined to a relatively narrow region. The early healing of rupture in this rupture scenario is caused by the short fault width (~ 5 km) [*Archuleta and Day*, 1980; *Day*, 1982a], instead of the rate dependence of friction proposed by *Heaton* [1990].

[22] The evolution of the rupture can also be observed from the evolution of shear stress and normal stress changes. Shear stress drops following the passage of the rupture front, and high stresses develop near the edges of the slipped area. Owing to the different velocity structure on each side of the fault, the normal stress on the fault is not constant. The normal stress variations have similar characteristics to a rupture on a bimaterial interface though the velocity structure in our simulation is more complicated; the normal stress varies as the rupture front progresses. In the positive direction (southeast), the normal stress change is compressive ahead of the rupture front, but tensile behind it, and vice versa in the negative direction (northwest, Figure 5). The normal stress variation is on the order of 1 MPa. Considering that the stress drop in most slipped areas other than the hypocentral region is on the order of 2 MPa, the material contrast has a nonnegligible effect on the rupture propagation; it effectively reduces the strength drop (yield stress minus dynamic frictional stress) in the negative direction and increases it in the positive direction.

[23] We show the time histories of slip rate, shear stress change, normal stress change, and shear stress change as a function of slip at five selected points along strike on the fault at the hypocentral depth (Figure 6). The component shown in this figure is along strike. The along-dip components are a factor of two orders smaller, thus negligible. Slip rate functions have a typical shape of crack-like solutions. There is no healing mechanism in the slip-weakening

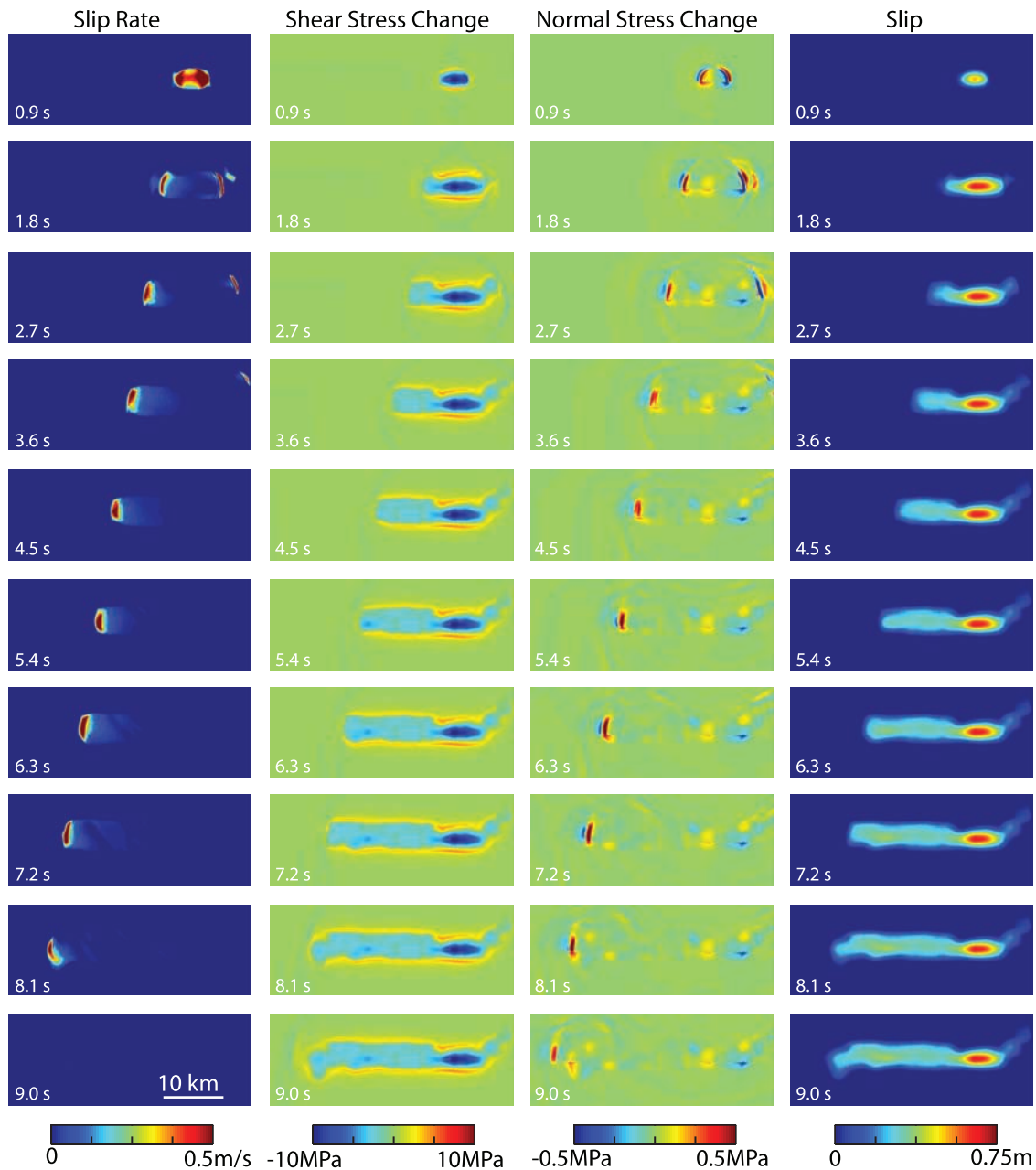


Figure 5. Snapshots of the preferred dynamic rupture model (Model B) for the 2004 Parkfield earthquake. Maps of the fault plane show contours of slip rate, shear stress change, normal stress change, and slip at 0.9 s intervals. The color scale is saturated. Rupture front propagates at nearly a constant speed in a narrow confined region. The early healing of the rupture is caused by the short fault width (~ 5 km).

friction law. The early healing of rupture is caused by the stopping phase arising from the fault edges. The slip rate is higher around the hypocenter due to a higher stress drop. Again, we see the characteristics of normal stress variations accompanying the rupture propagation in the negative direction. The shear stress change as a function of slip clearly follows the linear slip-weakening friction law. The breakdown zone at each point is well resolved with the element size of 100 m (Figure 6).

[24] The rupture velocity is well represented by an almost constant subshear velocity of 3.1 km/s toward the northwest and 3.0 km/s toward the southwest along the hypocentral

depth (Figure 7). Both these values are below the shear wave velocity on either side of fault at this depth (3.6 km/s on the southwest side and 3.2 km/s on the northeast side). However, the rupture propagates bilaterally with a much faster velocity in the first few seconds, about 4.3 km/s to the northwest and about 4.5 km/s to the southeast, exceeding the shear wave velocity of materials. The supershear transients can also be seen at 1.8 s in the slip rate panel of Figure 5. This large local rupture velocity is due to the large stress drop in the hypocentral region. The fact that high strength excess above and beneath the hypocentral asperity prevents the rupture from propagating vertically thus forces

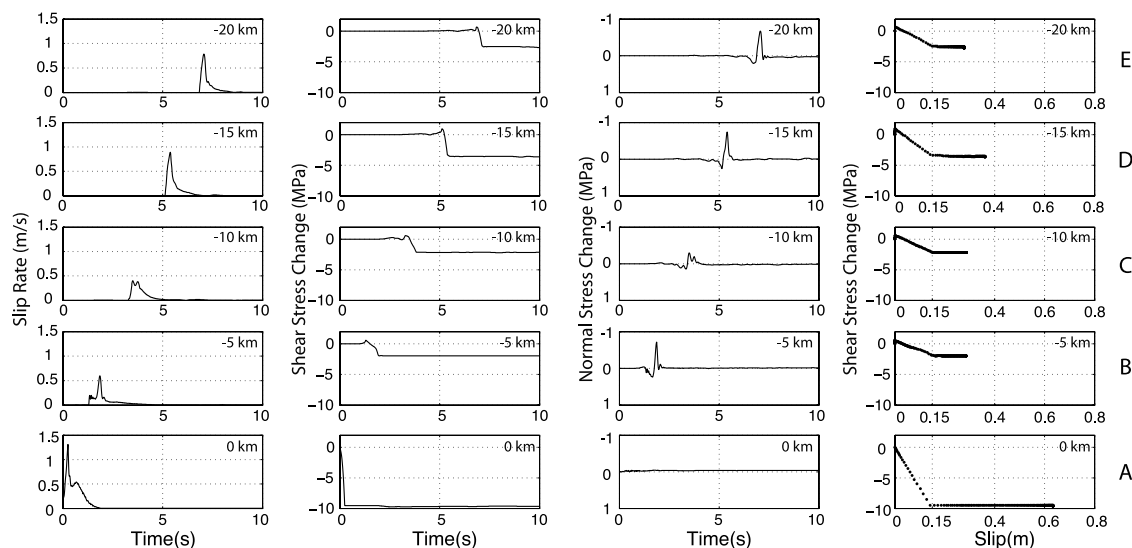


Figure 6. Plots of time histories of slip rate (first column), shear stress change (second column), normal stress change (third column), and shear stress change versus slip (fourth column) for five points located along-strike at the hypocentral depth northwest of the hypocenter for the preferred model (Model B). Slip rate, shear stress and slip are all shown in the along-strike direction. The distance to the hypocenter for each point is depicted in the upper right corner of each panel.

most of energy in the Mode II direction also facilitates the increase in the rupture velocity. However, supershear transients quickly die out due to the distribution of stress drop and strength excess in our dynamic model. The subshear rupture front carries most of the energy, which can be seen in the slip rate time history at Point B (Figure 6). The situation is different from the case where the stress conditions are homogeneous on the fault. Given homogeneous stress conditions, once the rupture goes to the supershear velocity, the supershear rupture front dominates the rupture propagation and causes dramatic differences in ground motions compared to a pure subshear rupture [Spudich and Frazer, 1984; Aagaard and Heaton, 2004; Dunham and Archuleta, 2004, 2005; Bernard and Baumont, 2005]. Local supershear rupture velocities associated with large stress drops have also been observed in other dynamic models [e.g., Day, 1982b; Olsen *et al.*, 1997; Peyrat *et al.*, 2001]. The supershear transients are rather short in our model; it is difficult to identify their signatures on the low-frequency (up to 1 Hz) near-source ground motions we use. Therefore we do not have constraints on whether the supershear rupture transients in our dynamic model are a robust feature or not.

[25] The results associated with the rupture propagation of Model A are shown in Figures S1–S3 in the auxiliary material¹. The rupture velocity, shear stress, and normal stress changes within the common area of both models are almost identical. The major difference between these two models is that the rupture of Model A broke a much wider area, a fault area very similar to what Custódio *et al.* [2005] found from the kinematic inversion. The wider fault width gives rise to a crack-like slip rate time function with rather long tails, which leads to a larger seismic moment, as we discuss in the following paragraph.

¹Auxiliary materials are available in the HTML. doi:10.1029/2007JB005216.

[26] The total seismic moment from our preferred dynamic model is 1.0×10^{18} Nm, corresponding to M_w 6.0. We calculate the moment by using $M_0 = \sum_i (G_{sw}^i d_{sw}^i - G_{ne}^i d_{ne}^i) A_i$, where G is the shear modulus, d is the displacement, A is subfault area, and subscripts sw and ne represents the southwest and northeast side of the fault, respectively. Owing to the material contrast, it is incorrect to assume that the displacement on either side of the fault is equal to

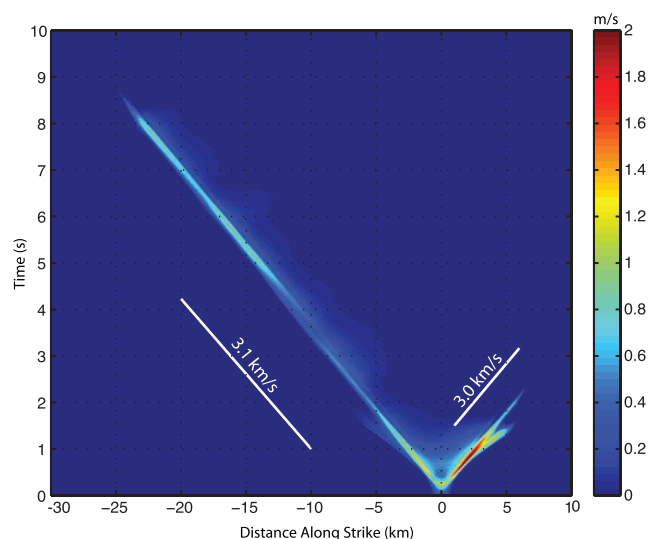


Figure 7. Time-space plot of the slip rate at the hypocentral depth for the preferred model (Model B). The main rupture front propagates at a velocity of about 3.1 km/s toward the northwest and 3.0 km/s to the southeast. Supershear transients can be seen in the first few seconds of the rupture. The material contrast causes the larger slip rate toward the southeast, which contributes to the large ground motions in Cholame.

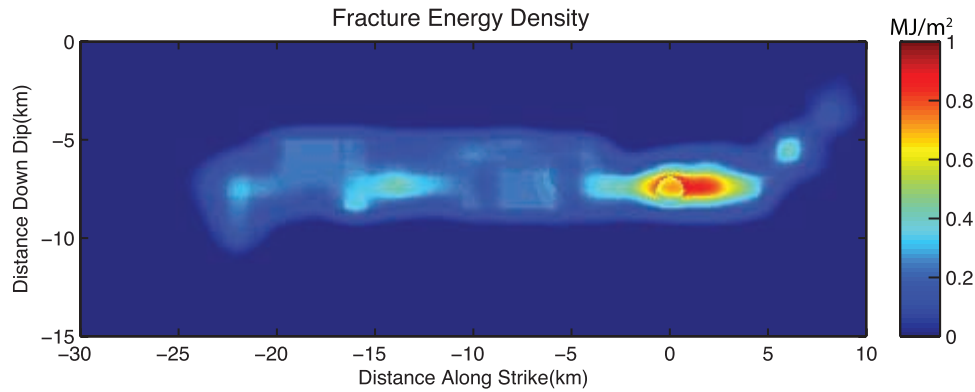


Figure 8. Distribution of fracture energy density (the energy lost to fracture per unit area) from the preferred dynamic model (Model B) is mapped onto the fault plane. See the text for details.

half of the slip. The seismic moment from Model A is 2.2×10^{18} Nm, about twice as much as that of the preferred model. Both the larger rupture area and the long tails of slip rate time histories contribute to the larger seismic moment. The long tail of the slip-rate time function affects little the ground motion but contributes significantly to the seismic moment.

[27] An advantage of a dynamic rupture model is that it permits the determination of the radiated energy and fracture energy of the earthquake [Favreau and Archuleta, 2003; Ma and Archuleta, 2006]. The radiated energy from our preferred dynamic model is 1.1×10^{13} J; the energy-to-moment ratio is 1.1×10^{-5} ; and the fracture energy is 3.0×10^{13} J. Following Gutenberg and Richter's relation for energy and magnitude, the radiated energy corresponds to a M 5.8, slightly less than the moment magnitude. For Model A, the radiated energy, the fracture energy, and the

energy-to-moment ratio are 1.8×10^{13} J, 5.3×10^{13} J, and 0.8×10^{-5} , respectively. The larger radiated energy (corresponding to a Gutenberg-Richter M 5.9) and fracture energy of Model A are again due to its larger rupture area. The distribution of fracture energy density (the energy lost to fracture per unit area in the slip-weakening friction law) strongly correlates with the stress drop (Figure 8 and Figure S4). This is because we used a uniform critical slip-weakening distance on the fault. The normal stress variations were taken into account in the calculation. The fracture energy density is maximum in the hypocentral region, and reaches 1 MJ/m^2 . A much smaller fracture energy density, less than 0.3 MJ/m^2 , is seen in the remaining slipped area.

[28] We compare the static shear stress changes from both Models A and B with the seismicity before and after the 2004 Parkfield main shock from 3 January 1984 to 30 June

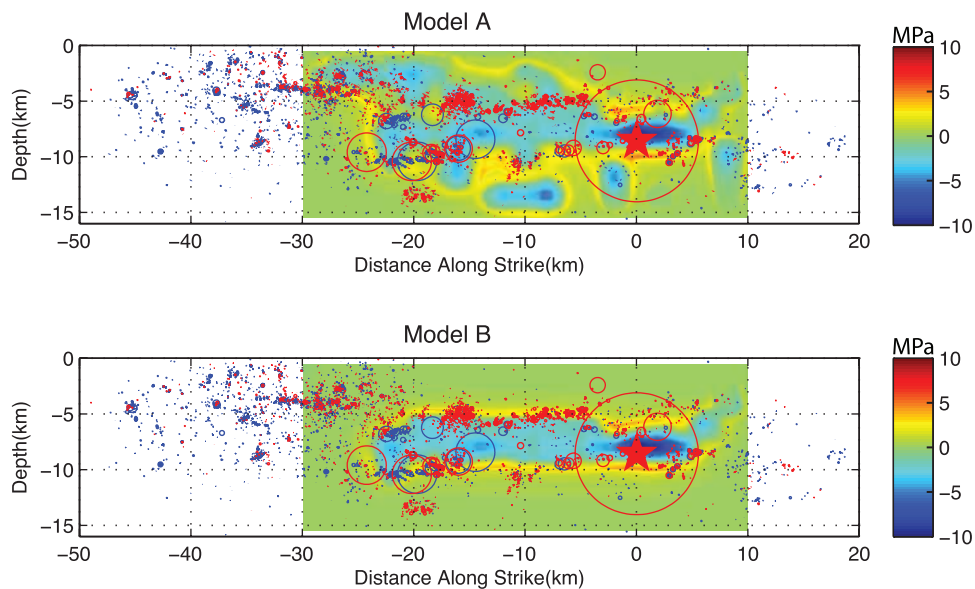


Figure 9. Seismicity before (blue) and after (red) the 2004 main shock from 1984 to 2005 [Thurber *et al.*, 2006] plotted on top of the stress change due to the main shock calculated from both dynamic models. The radius of earthquakes is calculated assuming a circular rupture area and a constant stress drop of 3 MPa. The correlation of stress increase with aftershock locations in Model B is due to that we limit the rupture area to be the area outlined by aftershock locations. However, very few aftershocks in the slipped area in Model B are likely due to the stress decrease during the main shock.

Table 2. Strong Motion Stations

Station	Longitude, degrees	Latitude, degrees	Epicentral Distance, km	Azimuth, degrees
C1e	-120.2750	35.7430	12.016	134.076
C2e	-120.2640	35.7520	12.117	127.409
C2w	-120.2900	35.7330	11.941	142.444
C3e	-120.2470	35.7700	12.380	115.680
C3w	-120.2960	35.7260	12.260	146.663
C4aw	-120.3160	35.7070	13.297	158.228
C4w	-120.3050	35.7170	12.707	152.205
COAL	-120.5900	36.0340	30.992	320.437
DFU	-120.4245	35.9392	14.225	340.043
EFU	-120.4212	35.8942	9.546	331.459
FFU	-120.4855	35.9111	14.578	314.748
FZ1	-120.3070	35.7580	8.823	139.401
FZ11	-120.3980	35.8960	8.933	343.950
FZ12	-120.4330	35.9000	10.637	328.084
FZ15	-120.4810	35.9210	15.099	318.791
FZ3	-120.3440	35.8030	2.950	125.571
FZ4	-120.3950	35.8360	2.933	311.380
FZ6	-120.4200	35.8590	6.323	315.212
FZ7	-120.4040	35.8710	6.549	332.625
FZ8	-120.3810	35.8780	6.657	351.904
FZ9	-120.4450	35.8790	9.483	314.986
GFU	-120.3464	35.8331	2.717	53.463
GH1w	-120.3780	35.8280	1.246	327.619
GH2e	-120.3480	35.8430	3.394	36.904
GH3e	-120.3340	35.8700	6.590	30.045
GH3w	-120.4110	35.7960	4.416	235.658
GH5w	-120.4770	35.7700	11.002	240.806
JFU	-120.4319	35.9397	14.518	337.644
KFU	-120.2025	35.7125	19.186	127.680
MFU	-120.4956	35.9576	19.088	323.861
PHOB	-120.4796	35.8666	11.182	298.493
RFU	-120.2535	35.6244	23.959	153.770
SC1e	-120.2940	35.7880	7.693	116.028
SC2e	-120.2820	35.8100	8.049	96.687
SC3e	-120.2700	35.8330	9.216	79.934
TEMB	-120.1690	35.7050	22.119	124.575
VC1w	-120.4970	35.9340	17.132	318.345
VC2e	-120.4670	35.9730	19.192	333.110
VC2w	-120.5090	35.9270	17.324	313.965
VC3w	-120.5340	35.9220	18.667	307.939
VC4w	-120.5510	35.9050	18.878	300.551
VC5w	-120.5650	35.8850	19.015	292.847
VFU	-120.5342	35.9225	18.715	308.037

2005 (Figure 9). For our preferred model most aftershocks fall on the edge of the rupture area where there is a shear stress increase, which is primarily due to our construction of the strength excess distribution (Figure 4) such that slip only occurs within the area outlined by aftershocks. There were very few aftershocks in the area where shear stress decreased due to the main shock, which suggests, however, that stress has likely played an important role in the aftershock distributions. Two M_w 5 aftershocks and one M_w 4.7 aftershock occurred near the edge of the slipped zone at 10 km depth northwest of the hypocenter and one M_w 4.7 aftershock occurred at 5 km depth southeast of the hypocenter. Seismicity after the main shock is dramatically higher in the northwest direction than in the southeast direction, consistent with the predominant rupture direction toward the northwest. Little seismicity before the main shock occurred within the rupture area of the preferred model as well, suggesting that this fault section has been locked. A 1994 M_w 5 earthquake occurred within the rupture area and three large earthquakes (a M_w 4.6 in 1992 and a M_w 4.5 and a M_w 5 in 1993) were on the edge

of the rupture area. There is an overlap in the microseismicity recorded before and after the main shock over the whole depth of the fault northwest of the ruptured area, presumably in the creeping section of the SAF. In Model A, however, the aftershock locations do not correlate well with the main shock stress changes; aftershocks occurred in the area where the shear stress decreased in the main shock.

3. Comparison Between Synthetics and Data

[29] Ground motions recorded at close distances from ruptured faults contain key information about the dynamics of faulting, having high sensitivity to the detailed rupture process. In engineering practice, near-source ground motions provide critical inputs for engineers to design structures near fault zones. Near-source ground motion records have historically been fairly scarce; therefore they remain extremely valuable.

[30] An unprecedented set of near-source ground motions was recorded with a dense array of accelerometers during the M_w 6.0 Parkfield earthquake. Eight stations were located

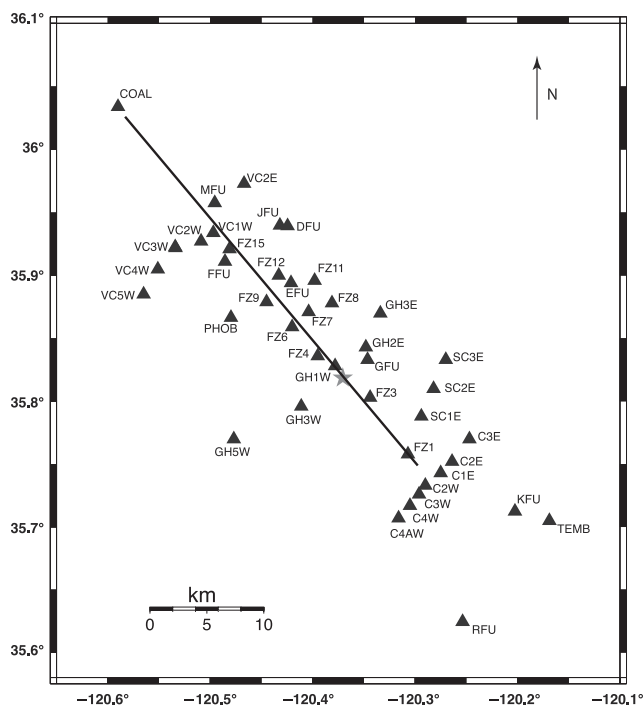


Figure 10. Map of near-source strong motion stations used in our dynamic modeling. The black line is the surface projection of the fault. The star denotes the epicenter.

within 1 km of the projected rupture trace and 40 stations were between 1 and 10 km from the projected rupture [Shakal et al., 2005; Bakun et al., 2005]. The total number of ground motion records obtained at these close distances was nearly doubled at a global scale by this single event. Thirteen continuous GPS stations located near the fault also recorded quality data during the main shock [Bakun et al., 2005; Harris and Arrowsmith, 2006]. This unique data set provides an unprecedented constraint on the rupture process during this earthquake.

[31] Ground motions at 43 stations (Table 2) are used to constrain our dynamic model. Figure 10 shows the station distribution. These data are the same data set as used by Custódio et al. [2005] in their kinematic inversion of the source model. All stations are located within 32 km of the epicenter and have a flat instrument response above 0.16 Hz.

[32] We compare some synthetics from our preferred dynamic model with recorded ground motions in Figure 11. (The more detailed comparison of synthetics of the dynamic model with synthetics of Custódio et al. [2005] and data at all 43 stations is shown in color in Figure S5.) All the data and synthetics are band-pass filtered between 0.16 Hz and 1 Hz. It can be seen that synthetics show satisfactory fits to the data. We plot all the stations on the same scale so that the rupture directivity can be clearly seen. Clear large fault-normal components are seen on both ends of the fault, especially in the Cholame stations (C4aw, C4w, C3w, C2e, and C3e) on the southeastern end of the fault. The fault-normal velocity is larger than the fault-parallel velocity at these stations, an indication of the dominant subshear rupture propagation toward the southeast. Fault-parallel velocities are larger than fault-normal velocities

near the hypocentral region, as clearly seen in the Stone Canyon stations (SC2e, SC3e) and Gold Hill stations (GH5w, GH3w, GFU, GH2e, and GH3e). This is largely due to the strong SH radiation from the hypocentral region. Fault-normal components are not well developed at such close distances to the hypocenter. Our synthetics do not fit well the reverberations in the late arrivals at the Vineyard Canyon stations (VC5w, VC4w, VC3w, VC2e, VFU, VC2W, and VC1W), which might be due to an oversimplification in our velocity model. However, we fit the early parts of the seismograms well. Good agreement in the three velocity components is even obtained at some stations very close to the fault (e.g., FZ8, FZ11, and FFU). At very close distances to the fault, the fault-parallel and vertical components are nearly nodal in a vertical strike-slip earthquake. Moreover, complicated velocity structure in the fault zone causes complex wave patterns [Cormier and Spudich, 1984]. Because of these factors, good fits to the data are hard to obtain at the stations very close to the fault. Still, we are able to fit well the pulse shapes of the fault-normal velocity component at some of the stations close to the fault (FZ6, VC1W, VC2W, and COAL).

[33] The misfit of our preferred model, found by calculating $\sum_{i=1}^{npts} \sum_{n=1}^{npts} (v_i^{syn}(t_n) - v_i^{data}(t_n))^2$ for all 43 stations, is $3.30 \text{ m}^2/\text{s}^2$, $5.66 \text{ m}^2/\text{s}^2$, and $0.91 \text{ m}^2/\text{s}^2$ for fault-parallel, fault-normal, and vertical velocity, respectively. Both synthetics and data were 18 s long and resampled at a time step of 0.1 s. The corresponding misfit found by inverting the data [Custódio et al., 2005] is $2.92 \text{ m}^2/\text{s}^2$, $4.67 \text{ m}^2/\text{s}^2$, and $1.14 \text{ m}^2/\text{s}^2$ for fault-parallel, fault-normal, and vertical velocity, respectively. The slightly worse misfit of the dynamic model comes largely from the Vineyard Canyon stations where we fail to fit the later reverberations. The good agreement between the synthetic and recorded ground motion suggests that our dynamic model is a fairly accurate representation of the rupture process. (The synthetics generated by Model A are shown in Figure S6. The misfit associated with this model is $3.94 \text{ m}^2/\text{s}^2$, $5.82 \text{ m}^2/\text{s}^2$, and $1.13 \text{ m}^2/\text{s}^2$ for fault-parallel, fault-normal, and vertical velocity, respectively.)

[34] In Figure 12, we show the peak surface velocity distributions for our preferred model (The surface peak velocity distribution of Model A is shown in Figure S7). Large fault-parallel motion, which consists largely of SH energy radiated from the hypocenter, is clearly observed near the epicenter. The SH wave radiation causes the large fault-parallel velocities at some Gold Hill and Stone Canyon stations shown in Figure 11. Strong fault-normal velocities are seen in both directions. The directivity effect of the rupture propagation contributes to the large ground motions at both ends of the fault where the fault-normal velocity is in general larger than the fault-parallel velocity. Besides both ends of the fault, the area near the town of Parkfield also experiences high fault-normal ground motions in our model, which is consistent with observations [Shakal et al., 2005]. We show snapshots of the three components of surface particle velocities in Figure S8.

[35] The coseismic offsets observed at 12 continuous GPS stations (Table 3) provide an independent check of the dynamic models because they are not involved in the trial-and-error modeling. We calculate the final displace-

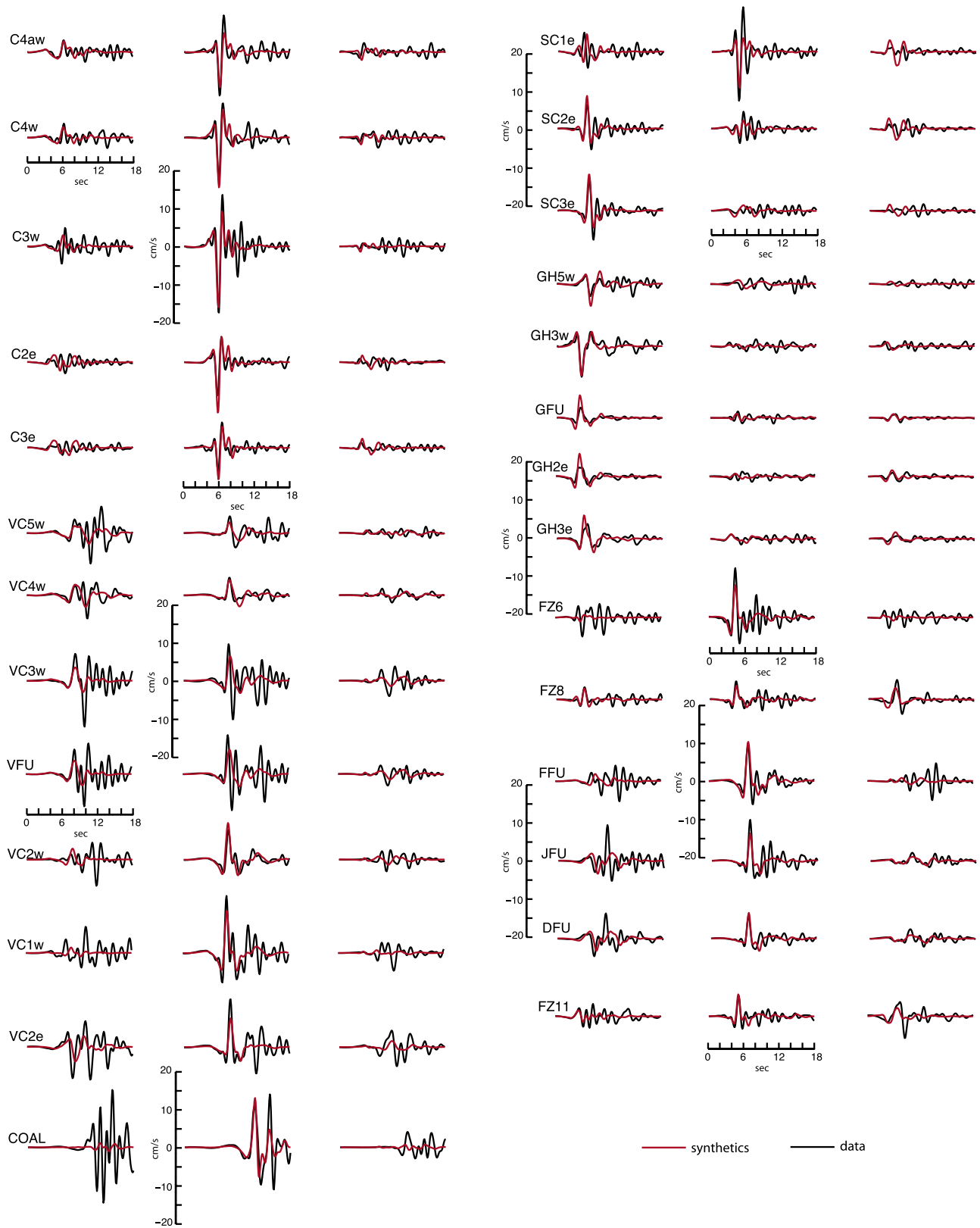


Figure 11. Comparison of velocity time histories between synthetics obtained from the preferred dynamic model (red) and observed near-source ground motions (black). For each station, the first component is fault-parallel, the second is fault-normal, and the third is vertical. All the waveforms are band-pass filtered between 0.16 and 1 Hz with a zero-phase, fourth-order Butterworth filter. The scale is the same for all stations.

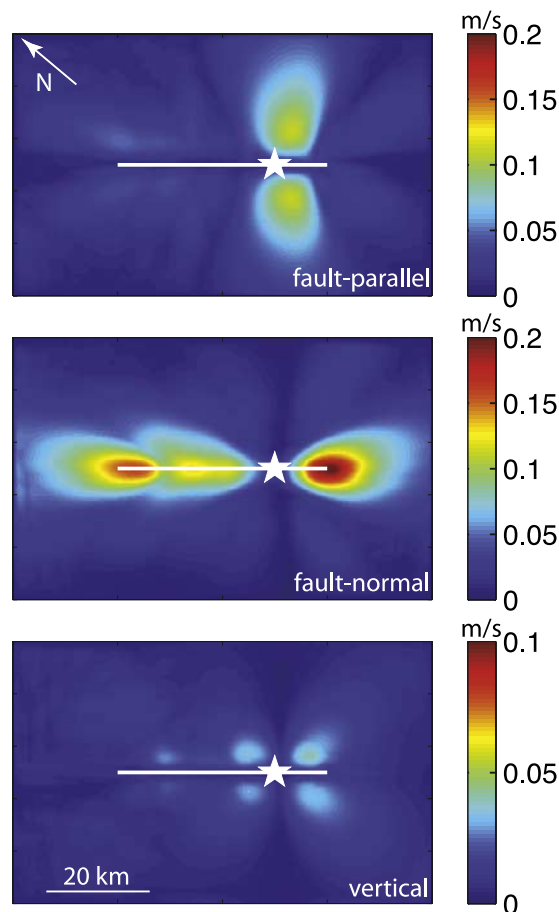


Figure 12. Distribution of the peak surface velocities from the preferred dynamic model (Model B). The color scale is saturated. The white line is the surface projection of the fault. The star denotes the epicenter. Large ground motions are located at both ends of the fault, consistent with observations.

ment field at the surface due to the slip from our preferred dynamic model in the velocity structure of Table 1 and compare the horizontal displacement vectors with the absolute GPS offset (Figure 13). We simply obtain the absolute GPS offsets by taking the difference of the averaged positions over 40 to 100 s after the main shock and 100 s before the main shock. The GPS position time series were

obtained as described by *Johnson et al.* [2006], following *Larson et al.* [2003] and adding modified sidereal filtering [*Choi et al.*, 2004]. For stations close to the fault, both fault geometry and complex velocity structure in the fault zone play important roles in determining the displacement vectors. The mismatch between the predicted displacement and data might indicate an oversimplification of the fault geometry and velocity structure. At stations away from the fault, we can fit the displacement amplitudes reasonably well; we can also fit the directions of displacement at some stations (such as TBLP). Note that the slip on our simple fault geometry can explain the displacement at station CARH, which is located on the southwest side of the main trace of the SAF but displaced coseismically toward the southeast. The deformation produced by Model A, however, overpredicts the GPS offsets by a factor of more than two (Figure S9).

4. Discussion

[36] Our preferred dynamic model bears some similarity to the quasi-dynamic model of the 1966 Parkfield earthquake [*Archuleta and Day*, 1980]; however, their model was constrained by only five strong motion stations. Slip occurred between 3 km and 9 km depths in their model, slightly shallower than our slip. The stress drop (2.5 MPa) and rupture velocity (3.1 km/s) in their model are also very similar to our fully dynamic model. The rupture area in our preferred model is delineated by the precise aftershock locations. The 5 km and 10 km depths might correspond to the transitions between a locked region (velocity-weakening) and a creeping region (velocity-strengthening). We considered a rupture model (A) that was more similar to the area where slip was found in the inversion by *Custódio et al.* [2005]. The major difference between Model A and Model B is the different rupture extent. While there is nothing to prevent the rupture from breaking into the creeping region, most coseismic slip should occur within the locked zone.

[37] Rupture velocity is one of the dominant factors affecting the ground motion in large earthquakes. In a dynamic model, we can control the rupture velocity by varying the stress drop and fracture energy [*Andrews*, 1976; *Guatteri and Spudich*, 2000] on the fault. We find that a rupture velocity on the order of 3 km/s in the first 2.0 s is necessary to account for the large ground motions at the Cholame stations. As we vary the strength excess and slip-

Table 3. Continuous GPS Stations

Station	Longitude, degrees	Latitude, degrees	Epicentral Distance, km	Azimuth, degrees
CAND	-120.43370	35.93935	14.949	335.519
CARH	-120.43082	35.88838	9.911	323.214
HOGS	-120.47949	35.86671	11.710	298.167
HUNT	-120.40238	35.88081	7.855	334.591
LAND	-120.47328	35.89979	13.419	313.317
LOWS	-120.59428	35.82871	20.714	273.604
MASW	-120.44306	35.83260	7.249	283.845
MIDA	-120.45883	35.92191	14.410	324.049
MNMC	-120.43405	35.96947	18.061	339.835
POMM	-120.47843	35.91991	15.348	318.210
RNCH	-120.52482	35.89999	17.112	302.634
TBLP	-120.36034	35.91741	11.173	362.155

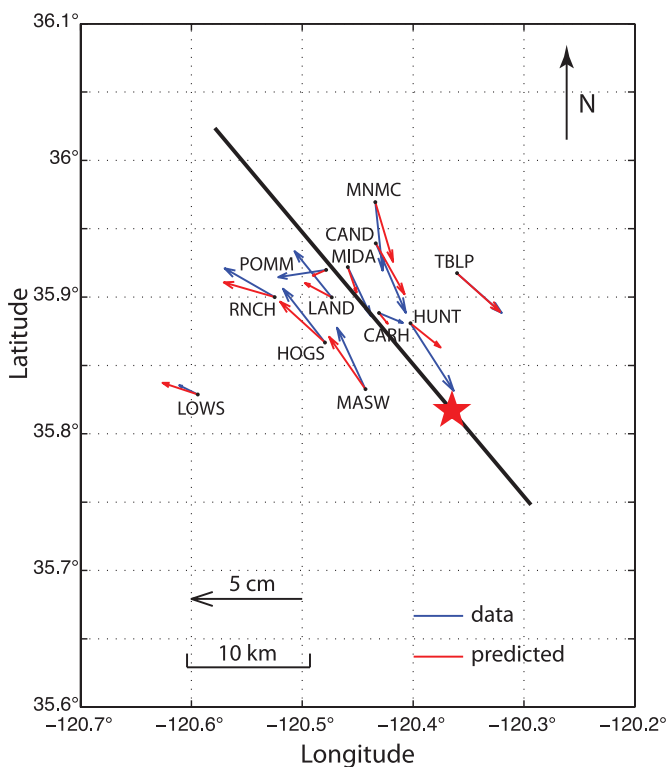


Figure 13. Comparison of the horizontal displacement predicted by the preferred model (Model B) with the absolute coseismic offsets recorded at 12 GPS stations. The long black line represents the surface projection of the fault. The star denotes the epicenter.

weakening distance in the hypocentral region to lower the rupture velocity, the fit with data worsens at the Cholame stations. The supershear transients in the dynamic model contribute little to the low-frequency ground motion (up to 1 Hz) at the Cholame stations because of their short durations. We also tried varying the rupture velocity to the northwest of the hypocenter. We find a worse fit to the data as we lower the rupture velocity. A slightly better fit is obtained instead when the rupture velocity is higher. By observing directly the propagation of displacement pulses at the surface *Borcherdt et al.* [2006] estimate an apparent rupture velocity of 2.86 ± 0.15 km/s (from fault-parallel pulses) and 3.03 ± 0.24 km/s (from fault-normal pulses), which are very similar to our rupture velocity. *Fletcher et al.* [2006] found a fast rupture velocity in the first 2.0 s of the rupture propagation and a slow rupture velocity afterward. They directly map the high-frequency arrivals recorded at UPSAR on the fault by using the apparent velocity and back azimuth of the arrivals. However, their rupture velocity decreases from an initial Rayleigh speed of the slower side of the fault to 2/3 of the shear wave speed of the slower side, which is inconsistent with our results. The difference is likely due to the different source locations on the fault of their high-frequency acceleration and our low-frequency velocity signals, and/or the large uncertainty in their analysis.

[38] The material contrast across the SAF plays a non-negligible role in the rupture propagation. In the negative direction (northwest), it unclamps the fault ahead of the rupture front but compresses the fault behind the rupture

front, resulting in a smaller strength drop and thus smaller ground motions. The 2004 Parkfield earthquake propagates predominantly in the negative direction. The normal stress variations are significant when compared to the shear stress changes on the fault in the simple velocity structure we use, where the shear wave velocity contrast is 12.5% at the hypocentral depth. The large ground motions recorded in Cholame can be attributed to the southeastward rupture propagation. This also corresponds to the positive direction of rupture propagation, where the normal stress change is compressive ahead of the rupture front but tensile behind it, resulting in a larger strength drop and ground motions. A clear asymmetry in the amplitude of slip velocity (larger in the southeast direction) is seen in Figure 7. The material contrast indeed caused a large effect on the ground motion recorded in Cholame.

[39] The 1966 M 6 earthquake propagated predominantly to the southeast [*Bakun and McEvilly*, 1979, 1984], which corresponds to the positive direction. The material contrast should have made significant effects on the rupture propagation and ground motions. However, it is difficult to identify these effects from strong motion data recorded at only a limited number of stations during this earthquake. The effects of material contrast should apply to all historical M 6 earthquakes in Parkfield; they all occurred on the same locked segment within almost the same velocity structure.

[40] If a dynamic rupture model and a kinematic rupture model can both explain the ground motion, are the rupture parameters in each rupture model consistent with each other? We compare the distributions of slip, rupture time and risetime on the fault between our preferred dynamic rupture model and the kinematic rupture model of *Custódio et al.* [2005] in Figure 14 (The comparison for Model A is shown in Figure S10). The slip distributions in the hypocentral region are similar. Our slip occurs between 5 km and 10 km depth, in a region outlined by aftershocks. There is shallow slip on the northwest corner of the fault in the kinematic model of *Custódio et al.* [2005]. However, shallow slip is not favored by the GPS data. In the GPS inversion of *Johanson et al.* [2006] and *Murray and Langbein* [2006], most slip is deep. By including the shallow asperity of *Custódio et al.* [2005], our Model A over-predicts the coseismic GPS offset. In fact, in the recent combined inversion of ground motion and GPS of *Custódio et al.* [2007], most slip takes place at depth, very similar to our preferred model.

[41] The distributions of rupture time and risetime are dramatically different between the dynamic model and the kinematic model. Rupture time and risetime are inherently dynamic features that can only be completely captured and resolved with dynamic rupture propagation, whereas they are not subject to the constraints posed by the elastodynamic equations yet highly variable in the kinematic model. The rupture time in the dynamic model is determined as the time when the along-strike slip rate exceeds 10^{-3} m/s at each point. The irregular rupture front in the kinematic rupture, which results from minimizing the misfit between synthetics and data while specifying a range of rupture time for each subfault, is likely unphysical. It is nontrivial to determine a local rupture velocity from the kinematic model.

[42] The risetime in the dynamic model is given by the time it takes for the slip to go from 10% to 90% of its final

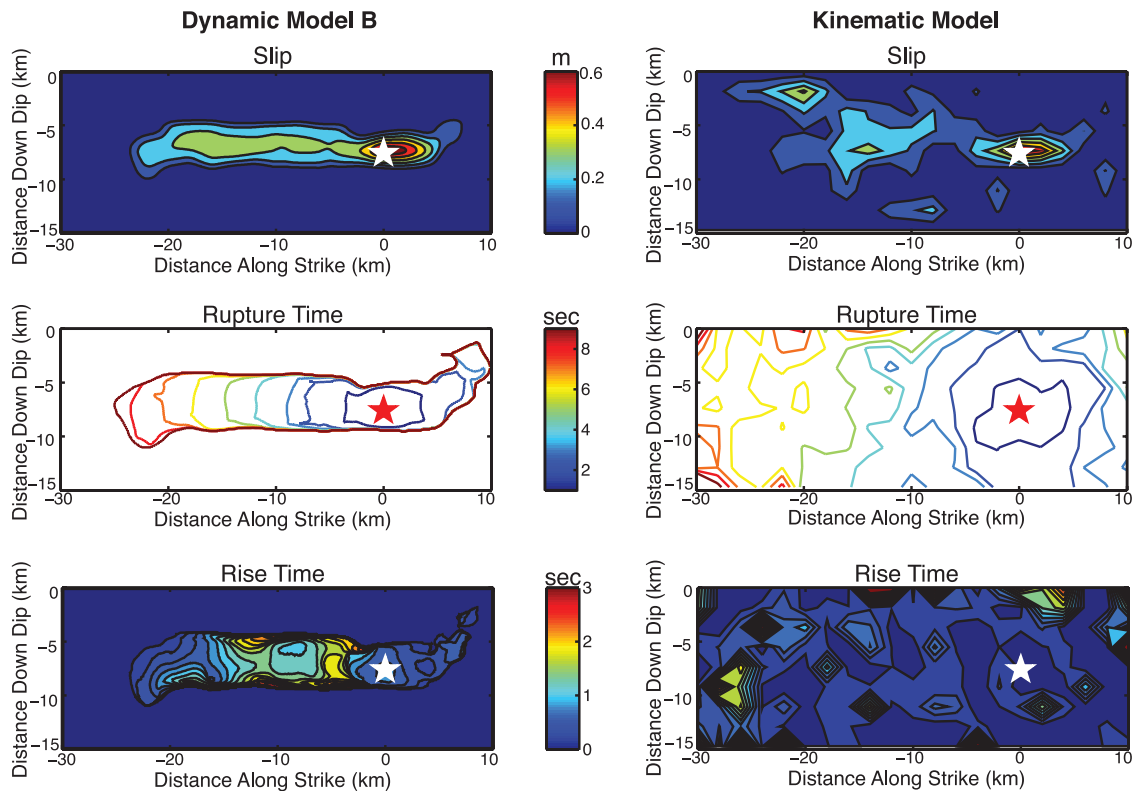


Figure 14. Comparison of the distributions of slip, rupture time and risetime calculated from our preferred dynamic model (Model B) and the kinematic model of *Custódio et al.* [2005]. The rupture time is plotted at a 1 s interval in both models. The risetime is plotted at 0.2 s intervals.

value at each point on the fault. We observe a risetime of 0.5–1.5 s on most of the slipped area. The short risetimes again are due to the small fault width (~ 5 km), which causes the healing of the rupture. In the kinematic model, risetime over most of the fault is less than 1.0 s, which is nearly unresolved and hence highly heterogeneous over the fault.

[43] The differences in the rupture parameters between the kinematic model and dynamic model suggest that many physical constraints can be obtained from the dynamic model and used in the kinematic inversion. This has been seen in the pseudo-dynamic modeling of rupture processes [e.g., *Guatteri et al.*, 2004].

[44] The radiated energy from the Parkfield earthquake is 1.1×10^{13} J based on the preferred dynamic model. No other energy estimate is yet available for this earthquake. Comparison of the energy-to-moment ratio from our dynamic model (1.1×10^{-5}) with that of the 1979 Imperial Valley earthquake (1.7×10^{-5} [*Favreau and Archuleta*, 2003]), 1994 Northridge earthquake (4.1×10^{-5} [*Ma and Archuleta*, 2006]), and 2002 Hector Mine earthquake (5×10^{-5} [*Venkataraman et al.*, 2002]) indicates that the 2004 Parkfield earthquake is a low apparent-stress event. This is consistent with the arguments of *Choy and Kirby* [2004] that mature faults have low apparent stress.

[45] With our preferred model, we have shown that the earthquake can be adequately modeled with most slip inside of the region delineated by the seismicity streaks. This is consistent with the argument of a locked zone at depth

surrounded by creeping zones [e.g., *Harris and Segall*, 1987; *Murray et al.*, 2001] and the interpretation of seismicity streaks as marking the transition zone between the locked zone and the creeping zone [*Nadeau et al.*, 1995]. The collocation of aftershocks of the 1966 and 2004 earthquakes with background seismicity has led to conclusions that fault rheology or geometry as opposed to the stress on the fault controls the distribution of seismicity [e.g., *Waldhauser et al.*, 2004; *Bakun et al.*, 2005; *Fletcher et al.*, 2006; *Johanson et al.*, 2006; *Langbein et al.*, 2006; *Murray and Langbein*, 2006; *Thurber et al.*, 2006]. However, the lack of seismicity within the locked zone since the 1966 M 6 earthquake does not invalidate the alternative explanation that the lack of seismicity was caused by the stress decrease during the 1966 and 2004 main shocks. The correlation of aftershock locations and the stress increase on the edge of the slipped area in our preferred model (Figure 9) is mainly due to our initial conditions that do not allow the slip to occur outside the area outlined by aftershock streaks. If the streaks do indeed mark the limits of the rupture area, one would expect a stress increase in the same region as the streaks. In fact, the seismicity rate increased dramatically inside the streaks after the 2004 main shock. The distinct frictional properties on fault could lead to different stress accumulation patterns during the interseismic period on the locked zone than those in the locked-creeping transition zone, which has led to the repeated M 6 earthquakes only on the locked zone. Thus it

is very likely that both the fault rheology and stress on the fault control the distribution of seismicity on the SAF near Parkfield.

5. Conclusions

[46] We have presented two dynamic rupture models of the 2004 Parkfield earthquake. The preferred dynamic model with slip bounded by seismicity streaks explains the large amount of near-source ground motions and coseismic GPS offsets. This model confirms a locked zone at depth and is consistent with the interpretation that seismicity streaks in Parkfield mark the transition zone between a creeping zone and a locked zone on the fault.

[47] Stress drop in the hypocentral region during the main shock reaches 10 MPa. It causes the strong bilateral rupture propagation in the first few seconds of rupture. The stress drop in asperities away from the hypocenter is on the order of 2 MPa. Material contrasts across the SAF cause significant normal stress variations (~ 1 MPa) on the fault, which leads to a larger strength drop to the southeast direction and a smaller strength drop to the northwest. The larger strength drop contributes to the large ground motion recorded in Cholame.

[48] The main rupture front propagates over most of the fault at a nearly constant subshear velocity of about 3.1 km/s toward the northwest and 3.0 km/s to the southeast. The bilateral rupture propagation contributes to the large ground motions both in the northwest and southeast directions. The dramatic differences in the dynamic and kinematic rupture parameters suggest that dynamic rupture models can provide physical constraints to the kinematic inversions.

[49] The radiated energy from the Parkfield earthquake determined from the preferred dynamic model is 1.1×10^{13} J. The fracture energy is 3.0×10^{13} J, a nonnegligible portion of the total energy release. The energy-to-moment ratio is 1.1×10^{-5} ; this relatively low ratio suggests that the Parkfield segment of the SAF is mature [Choy and Kirby, 2004]. Very few aftershocks of the 2004 earthquake as well as the 1966 M 6 earthquake occurred within the area bounded by seismicity streaks, suggesting the important role of stress on the distribution of seismicity in the locked zone. Both the fault rheology and stress on fault likely control the distribution of seismicity on the Parkfield section of the SAF.

[50] **Acknowledgments.** The first author wishes to thank Paul Spudich, Ruth Harris, and Greg Beroza for many insightful discussions. The constructive reviews from Clifford Thurber (associate editor), Steven Day, and Arben Pitarka have dramatically improved the manuscript. Kristine M. Larson kindly provided us the processed GPS time series. This work is supported by National Science Foundation (EAR-0512000), the Southern California Earthquake Center (SCEC), NSF ITR through the award EAR-0122464 (The SCEC Community Modeling Environment (SCEC/CME): An Information Infrastructure for System-Level Earthquake Research), and IGPP LANL grant 04-08-16L-1532. SCEC is funded by NSF Cooperative Agreement EAR-0106924 and USGS Cooperative Agreement 02HQAG0008. S. Custódio acknowledges a Ph.D. fellowship (SFRH/BD/14353/2003) from Fundação para a Ciência e Tecnologia (Portuguese Foundation for Science and Technology). This is SCEC contribution 1088 and Institute for Crustal Studies contribution 0806.

References

Aagaard, B. T., and T. H. Heaton (2004), Near-source ground motions from simulations of sustained intersonic and supersonic fault ruptures, *Bull. Seismol. Soc. Am.*, *94*, 2064–2078.

Andrews, D. J. (1976), Rupture velocity of plane strain shear cracks, *J. Geophys. Res.*, *81*, 5679–5687.

Andrews, D. J. (1999), Test of two methods for faulting in finite-difference calculations, *Bull. Seismol. Soc. Am.*, *89*, 931–937.

Andrews, D. J., and Y. Ben-Zion (1997), Wrinkle-like slip pulse on a fault between different materials, *J. Geophys. Res.*, *102*, 553–571.

Archuleta, R. J., and S. M. Day (1980), Dynamic rupture in a layered medium: The 1966 Parkfield earthquake, *Bull. Seismol. Soc. Am.*, *70*, 671–689.

Bakun, W. H., and T. V. McEvilly (1979), Earthquakes near Parkfield, California: Comparing the 1934 and 1966 sequences, *Science*, *205*, 1375–1377.

Bakun, W. H., and T. V. McEvilly (1984), Recurrence models and Parkfield, California, earthquakes, *J. Geophys. Res.*, *89*, 3051–3058.

Bakun, W. H., et al. (2005), Implications for prediction and hazard assessment from the 2004 Parkfield earthquake, *Nature*, *437*, 969–974.

Ben-Zion, Y. (2006), Comment on “Material contrast does not predict earthquake rupture propagation direction” by R. A. Harris and S. M. Day, *Geophys. Res. Lett.*, *33*, L13310, doi:10.1029/2005GL025652.

Ben-Zion, Y., and D. J. Andrews (1998), Properties and implications of dynamic rupture along a material interface, *Bull. Seismol. Soc. Am.*, *88*, 1085–1094.

Bernard, P., and D. Baumont (2005), Shear mach wave characterization for kinematic fault rupture models with constant supershear rupture velocity, *Geophys. J. Int.*, *162*, 431–447.

Borcherdt, R. D., J. Malcolm, S. Johnston, G. Glassmoyer, and C. Dietel (2006), Recordings of the 2004 Parkfield earthquake on the general earthquake observation system array: Implications for earthquake precursors, fault rupture, and coseismic strain changes, *Bull. Seismol. Soc. Am.*, *96*, S73–S89, doi:10.1785/0120050827.

Choi, K., A. Bilich, K. M. Larson, and P. Axelrad (2004), Modified sidereal filtering: Implications for high-rate GPS positioning, *Geophys. Res. Lett.*, *31*, L22608, doi:10.1029/2004GL021621.

Choy, G. L., and S. H. Kirby (2004), Apparent stress, fault maturity and seismic hazard for normal-fault earthquakes at subduction zones, *Geophys. J. Int.*, *159*, 991–1012.

Cochard, A., and J. R. Rice (2000), Fault rupture between dissimilar materials: Ill-posedness, regularization, and slip-pulse response, *J. Geophys. Res.*, *105*, 25,891–25,907.

Cormier, V. F., and P. Spudich (1984), Amplification of ground motion and waveform complexities in fault zones: Examples from the San Andreas and Calaveras faults, *Geophys. J. R. Astron. Soc.*, *79*, 135–152.

Custódio, S., P. Liu, and R. J. Archuleta (2005), The 2004 M_w 6.0 Parkfield, California, earthquake: Inversion of near-source ground motion using multiple data sets, *Geophys. Res. Lett.*, *32*, L23312, doi:10.1029/2005GL024417.

Custódio, S., M. T. Page, K. Larson, and R. J. Archuleta (2007), Combining different datasets to obtain a rupture model: The 2004 M6.0 Parkfield, California, earthquake, *Seismol. Res. Lett.*, *78*, 303.

Dalguer, L. A., K. Irikura, and J. D. Riera (2003), Generation of new cracks accompanied by the dynamic shear rupture propagation of 2000 Tottori (Japan) earthquake, *Bull. Seismol. Soc. Am.*, *93*, 2236–2252.

Das, S., and K. Aki (1977), A numerical study of two-dimensional spontaneous rupture propagation, *Geophys. J. R. Astron. Soc.*, *50*, 643–668.

Day, S. M. (1982a), Three-dimensional finite difference simulation of fault dynamics: Rectangular faults with fixed rupture velocity, *Bull. Seismol. Soc. Am.*, *72*, 705–727.

Day, S. M. (1982b), Three-dimensional simulation of spontaneous rupture: The effect of nonuniform prestress, *Bull. Seismol. Soc. Am.*, *72*, 1881–1902.

Day, S. M., and G. P. Ely (2002), Effect of a shallow weak zone on fault rupture: Numerical simulation of scale-model experiments, *Bull. Seismol. Soc. Am.*, *92*, 3022–3041.

Day, S. M., L. A. Dalguer, N. Lapusta, and Y. Liu (2005), Comparison of finite difference and boundary integral solutions to three-dimensional spontaneous rupture, *J. Geophys. Res.*, *110*, B12307, doi:10.1029/2005JB003813.

Dor, O., Y. Ben-Zion, T. K. Rockwell, and J. Brune (2006a), Pulverized rocks in the Mojave section of the San Andreas Fault zone, *Earth Planet. Sci. Lett.*, *245*, 642–654.

Dor, O., T. K. Rockwell, and Y. Ben-Zion (2006b), Geologic observations of damage asymmetry in the structure of the San Jacinto, San Andreas and Punchbowl faults in southern California: A possible indicator for preferred rupture propagation direction, *Pure Appl. Geophys.*, *163*, 301–349, doi:10.1007/s00024-005-0023-9.

Dunham, E. M., and R. J. Archuleta (2004), Evidence for a supershear transient during the 2002 Denali Fault earthquake, *Bull. Seismol. Soc. Am.*, *94*, S256–S268.

Dunham, E. M., and R. J. Archuleta (2005), Near-source ground motion from steady state dynamic rupture pulses, *Geophys. Res. Lett.*, *32*, L03302, doi:10.1029/2004GL021793.

- Eberhart-Phillips, D., and A. J. Michael (1993), Three-dimensional velocity structure, seismicity, and fault structure in the Parkfield region, central California, *J. Geophys. Res.*, *98*, 15,737–15,758.
- Favreau, P., and R. J. Archuleta (2003), Direct seismic energy modeling and an application to the 1979 Imperial Valley earthquake, *Geophys. Res. Lett.*, *30*(5), 1198, doi:10.1029/2002GL015968.
- Fletcher, J. B., P. Spudich, and L. M. Baker (2006), Direct observation of earthquake rupture propagation in the 2004 Parkfield, California, earthquake using the UPSAR accelerograph array, *Bull. Seismol. Soc. Am.*, *96*, S129–S142, doi:10.1785/0120050812.
- Guatteri, M., and P. Spudich (1998), Coseismic temporal changes of slip direction: The effect of absolute stress on dynamic rupture, *Bull. Seismol. Soc. Am.*, *88*, 777–789.
- Guatteri, M., and P. Spudich (2000), What can strong-motion data tell us about slip-weakening fault-friction laws?, *Bull. Seismol. Soc. Am.*, *90*, 98–116.
- Guatteri, M., P. M. Mai, and G. C. Beroza (2004), A pseudo-dynamic approximation to dynamic rupture models for strong motion prediction, *Bull. Seismol. Soc. Am.*, *94*, 2051–2063.
- Harris, R. A., and J. R. Arrowsmith (2006), Introduction to the special issue on the 2004 Parkfield earthquake and the Parkfield Earthquake Prediction Experiment, *Bull. Seismol. Soc. Am.*, *96*, S1–S10, doi:10.1785/0120050831.
- Harris, R. A., and S. M. Day (1997), Effects of a low-velocity zone on a dynamic rupture, *Bull. Seismol. Soc. Am.*, *87*, 1267–1280.
- Harris, R. A., and S. M. Day (2005), Material contrast does not predict earthquake rupture propagation direction, *Geophys. Res. Lett.*, *32*, L23301, doi:10.1029/2005GL023941.
- Harris, R. A., and S. M. Day (2006), Reply to comment by Y. Ben-Zion on “Material contrast does not predict earthquake rupture propagation direction,” *Geophys. Res. Lett.*, *33*, L13311, doi:10.1029/2006GL026811.
- Harris, R. A., and P. Segall (1987), Detection of a locked zone at depth on the Parkfield, California, segment of the San Andreas fault, *J. Geophys. Res.*, *92*, 7945–7962.
- Heaton, T. H. (1990), Evidence for and implications of self-healing pulses of slip in earthquake rupture, *Phys. Earth Planet. Int.*, *64*, 1–20.
- Ida, Y. (1972), Cohesive force across the tip of a longitudinal-shear crack and Griffith’s specific surface energy, *J. Geophys. Res.*, *77*, 3796–3805.
- Johanson, I. A., E. J. Fieding, F. Rolandone, and R. Burgmann (2006), Coseismic and postseismic slip of the 2004 Parkfield earthquake from space-geodetic data, *Bull. Seismol. Soc. Am.*, *96*, S269–S282, doi:10.1785/0120050818.
- Johnson, K. M., R. Burgmann, and K. Larson (2006), Frictional properties on the San Andreas Fault near Parkfield, California, inferred from models of afterslip following the 2004 earthquake, *Bull. Seismol. Soc. Am.*, *96*, S321–S338, doi:10.1785/0120050808.
- Langbein, J., R. Borchardt, D. Dreger, J. Fletcher, J. L. Hardebeck, M. Hellweg, C. Ji, M. Johnston, J. R. Murray, and R. Nadeau (2005), Preliminary report on the 28 September 2004, M 6.0 Parkfield, California earthquake, *Seismol. Res. Lett.*, *76*, 10–26.
- Langbein, J., J. R. Murray, and H. A. Snyder (2006), Coseismic and initial postseismic deformation from the 2004 Parkfield, California, earthquake, observed by Global Positioning System, Electronic Distance Meter, creepmeters, and borehole strainmeters, *Bull. Seismol. Soc. Am.*, *96*, S304–S320.
- Larson, K. M., P. Bodin, and J. Gombert (2003), Using 1–Hz GPS Data to measure deformations caused by the Denali fault earthquake, *Science*, *300*(5624), 1421–1424, doi:10.1126/science.1084531.
- Liu, P., S. Custódio, and R. J. Archuleta (2006), Kinematic inversion of the 2004 M_w 6.0 Parkfield earthquake including an approximation to site effects, *Bull. Seismol. Soc. Am.*, *96*, S143–S158, doi:10.1785/0120050826.
- Lysmer, J., and R. L. Kuhlemeyer (1969), Finite dynamic model for infinite media, *J. Eng. Mech.*, *95*, 859–877.
- Ma, S., and R. J. Archuleta (2006), Radiated seismic energy based on dynamic rupture models of faulting, *J. Geophys. Res.*, *111*, B05315, doi:10.1029/2005JB004055.
- Ma, S., and P. Liu (2006), Modeling of the perfectly matched layer absorbing boundaries and intrinsic attenuation in explicit finite element methods, *Bull. Seismol. Soc. Am.*, *96*, 1779–1794, doi:10.1785/0120050219.
- Murray, J., and J. Langbein (2006), Slip on the San Andreas Fault at Parkfield, California, over two earthquake cycles and the implications for seismic hazard, *Bull. Seismol. Soc. Am.*, *96*, S283–S303, doi:10.1785/0120050820.
- Murray, J., P. Segall, P. Cervelli, W. Prescott, and J. Svarc (2001), Inversion of GPS data for spatially variable slip-rate on the San Andreas fault near Parkfield, *Geophys. Res. Lett.*, *28*, 359–362.
- Nadeau, R. M., W. Foxall, and T. V. McEvilly (1995), Clustering and periodic recurrence of microearthquakes on the San Andreas Fault at Parkfield, California, *Science*, *267*, 503–507.
- Nielsen, S. B., and K. B. Olsen (2000), Constraints on stress and friction from dynamic rupture models of the 1994 Northridge, California, earthquake, *Pure Appl. Geophys.*, *157*, 2029–2046.
- Olsen, K., R. Madariaga, and R. J. Archuleta (1997), Three dimensional dynamic simulation of the 1992 Landers earthquake, *Science*, *278*, 834–838.
- Palmer, A. C., and J. R. Rice (1973), The growth of slip surfaces in the progressive failure of over-consolidated clay, *Proc. R. Soc. London, Ser. A*, *332*, 527–548.
- Peyrat, S., and K. B. Olsen (2004), Nonlinear dynamic rupture inversion of the 2000 Western Tottori, Japan, earthquake, *Geophys. Res. Lett.*, *31*, L05604, doi:10.1029/2003GL019058.
- Peyrat, S., K. Olsen, and R. Madariaga (2001), Dynamic modeling of the 1992 Landers earthquake, *J. Geophys. Res.*, *106*, 26,467–26,482.
- Ranjith, K., and J. R. Rice (2001), Slip dynamics at an interface between dissimilar materials, *J. Mech. Phys. Solids*, *49*, 341–361.
- Rubin, A. M., and J.-P. Ampuero (2007), Aftershock asymmetry on a bimaterial interface, *J. Geophys. Res.*, *112*, B05307, doi:10.1029/2006JB004337.
- Shakal, A., V. Graizer, M. Huang, R. Borchardt, H. Haddadi, K.-W. Lin, C. Stephens, and P. Roffers (2005), Preliminary analysis of strong-motion recordings from the 28 September 2004 Parkfield, California earthquake, *Seismol. Res. Lett.*, *76*, 27–39.
- Simpson, R. W., M. Barall, J. Langbein, J. R. Murray, and M. J. Rymer (2006), San Andreas Fault geometry in the Parkfield, California, region, *Bull. Seismol. Soc. Am.*, *96*, S28–S37, doi:10.1785/0120050824.
- Spudich, P., and L. N. Frazer (1984), Use of ray theory to calculate high-frequency radiation from earthquake sources having spatially-variable rupture velocity and stress drop, *Bull. Seismol. Soc. Am.*, *74*, 2061–2082.
- Thurber, C., S. Roecker, K. Roberts, M. Gold, L. Powell, and K. Ritterger (2003), Earthquake locations and three-dimensional fault zone structure along the creeping section of the San Andreas fault near Parkfield, CA: Preparing for SAFOD, *Geophys. Res. Lett.*, *30*(3), 1112, doi:10.1029/2002GL016004.
- Thurber, C., H. Zhang, F. Waldhauser, J. Hardebeck, A. Michael, and D. Eberhart-Phillips (2006), Three-dimensional compressional wave-speed model, earthquake relocations, and focal mechanisms for the Parkfield, California, region, *Bull. Seismol. Soc. Am.*, *96*, S38–S49, doi:10.1785/0120050825.
- Venkataraman, A., L. Rivera, and H. Kanamori (2002), Radiated energy from the 16 October 1999 Hector Mine earthquake: Regional and teleseismic estimates, *Bull. Seismol. Soc. Am.*, *92*, 1256–1265.
- Waldhauser, F., W. Ellsworth, D. P. Schaff, and A. Cole (2004), Streaks, multiplets, and holes: High-resolution spatio-temporal behavior of Parkfield seismicity, *Geophys. Res. Lett.*, *31*, L18608, doi:10.1029/2004GL020649.
- Xia, K., A. J. Rosakis, H. Kanamori, and J. R. Rice (2005), Laboratory earthquake along inhomogeneous faults: Directionality and supershear, *Science*, *308*, 681–684, doi:10.1126/science.1108193.

R. J. Archuleta, S. Custódio, and P. Liu, Department of Earth Science and Institute for Crustal Studies, University of California, Santa Barbara, Santa Barbara, CA 93106, USA.

S. Ma, Department of Geophysics, Stanford University, Stanford, CA 94305, USA. (shuoma@stanford.edu)